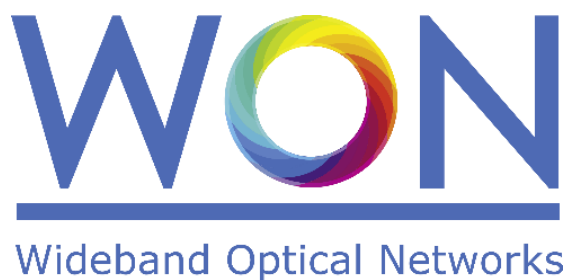


Marie Skłodowska-Curie (MSCA) – Innovative Training Networks (ITN)
H2020-MSCA-ITN European Training Networks



Wideband Optical Networks [WON]

Grant agreement ID: 814276

WP3 – In-line components design

**Deliverable D3.5 Evaluation results of wideband WSS and multicast
mux/de-mux**



This project has received funding from the European Union's Horizon 2020 research and innovation programme under the Marie Skłodowska-Curie grant agreement 814276.

Document Details

| | |
|-----------------------|---|
| Work Package | WP3 – In-line components design |
| Deliverable number | D3.5 |
| Deliverable Title | Evaluation results of wideband WSS and multicast mux/de-mux |
| Lead Beneficiary: | Technische Universiteit Eindhoven (TUE) |
| Deliverable due date: | 31 December 2021 |
| Actual delivery date: | 31 March 2022 |
| Dissemination level: | Public |

Project Details

| | |
|----------------------|---|
| Project Acronym | WON |
| Project Title | Wideband Optical Networks |
| Call Identifier | H2020-MSCA-2018 Innovative Training Networks |
| Coordinated by | Aston University, UK |
| Start of the Project | 1 January 2019 |
| Project Duration | 48 months |
| WON website: | https://won.astonphotonics.uk/ |
| CORDIS Link | https://cordis.europa.eu/project/rcn/218205/en |

WON Consortium and Acronyms

| Consortium member | Legal Entity Short Name |
|--|-------------------------|
| Aston University | Aston |
| Danmarks Tekniske Universitet | DTU |
| VPIphotonics GmbH | VPI |
| Infinera Portugal | INF PT |
| Fraunhofer HHI | HHI |
| Politecnico di Torino | POLITO |
| Technische Universiteit Eindhoven | TUE |
| Universiteit Gent | UG |
| Keysight Technologies | Keysight |
| Finisar Germany GmH | Finisar |
| Orange SA | Orange |
| Technische Universitaet Berlin | TUB |
| Instituto Superior Tecnico, University of Lisboa | IST |

Abbreviations

| | |
|---------|--|
| ADC: | Analog to digital converter |
| APD: | Avalanche Photodiode |
| ASE: | Amplified spontaneous emission |
| AWG: | Arrayed waveguide gratings |
| BER: | Bit error rate |
| CW: | Continuous Wave |
| DAC: | Digital to analog converter |
| ER: | Extinction Ratio |
| ETN: | European Training Network |
| FSR: | Free spectral range |
| IM/DD: | Intensity Modulation/Direct Detection |
| MZI: | Mach-Zehnder interferometer |
| NGMI: | Normalized generalized mutual information |
| OSNR: | Optical signal to noise ratio |
| OXC: | Optical Cross Connect |
| PDL: | Polarization dependent losses |
| PDWS: | Polarization dependent wavelength shift |
| PECVD: | Plasma enhanced chemical vapor deposition |
| QAM: | Quadrature amplitude modulation |
| ROADMs: | Reconfigurable optical add drop multiplexers |
| SOA: | Semiconductor Optical Amplifier |
| TLS: | Tunable laser source |
| VOA: | Variable Optical Attenuator |
| WDM: | Wavelength Division Multiplexing |
| WSS: | Wavelength Selective Switch |

CONTENTS

| | |
|--|----|
| LIST OF FIGURES | 5 |
| LIST OF TABLES | 5 |
| EXECUTIVE SUMMARY | 6 |
| 1. WSS and Mux/demux overview | 6 |
| 2. Wideband wavelength selective switch | 6 |
| 2.1 Introduction | 6 |
| 2.2 WSS multiband operation | 7 |
| 2.3 WSS employed in a wideband data transmission | 10 |
| 3. Ultrawide-band mux/demux based on polarization insensitive arrayed waveguide gratings | 14 |
| 3.1 Introduction | 14 |
| 3.2 Design and Fabrication..... | 14 |
| 3.3 Experimental characterization | 16 |
| 4. Conclusions | 22 |
| 5. REFERENCES | 23 |

LIST OF FIGURES

| | |
|--|----|
| Figure 1: Multi-band 2-degree switching node | 6 |
| Figure 2: Layout of the fabricated device | 7 |
| Figure 3: Experimental setup for channel measurement across the multiband spectrum. | 7 |
| Figure 4: Passband shape of the AWG | 8 |
| Figure 5: Extra 13.7 dB losses in the O-band due to the wavelength couplers. | 8 |
| Figure 6- Filter shapes for O, S, C and L-bands. | 9 |
| Figure 7: ER across channels in the O, S, C and L-bands. | 9 |
| Figure 8: NRZ-OOK Experimental setup. | 10 |
| Figure 9: Bit error rate results with 10 Gb/s NRZ-OOK data for the O and S-band. | 11 |
| Figure 10: BER results with 35 Gb/s in the C and L-band. | 11 |
| Figure 11: Schematic of the coherent experimental setup. | 12 |
| Figure 12: Averaged NGMI and BER for the S, C and L-bands. | 12 |
| Figure 13: OSNR penalty from the S to the L-band for NGMI values of 0.88 and 0.92, corresponding net data-rates of 161.84 Gb/s and 169.83 Gb/s respectively. | 13 |
| Figure 14: (a) Schematic of hybrid WSS. (b) Micrograph of the fabricated hybrid-assembly 1 x 1 WSS | 14 |
| Figure 15: Detailed structure of the 3 – μ m Silicon strip waveguide. | 15 |
| Figure 16: (a) AWG Layout. (b) Simulated 12 channels output for TE and TM modes in the C-band. | 16 |
| Figure 17: Micrograph of the fabricated AWG. | 16 |
| Figure 18: Experimental setup for characterization of the 1 x 2 PI AWG. | 17 |
| Figure 19: Measured output spectra of 12 channels at the O, E, S band, and the respective PDWs, PDLs ... | 18 |
| Figure 20: Measured output spectra of 12 channels at the C, L-band and the respective PDWs and PDLs. .. | 18 |
| Figure 21: BER curves vs received power of the TE and TM modes at 1548.40 nm for (a) 10 Gb/s, (b) 20 Gb/s and (c) 35 Gb/s, and channel penalties at (d) 10 Gb/s, (e) 20 Gb/s and (f) BER curve of TE and TM modes for WDM 10 Gb/s signal. | 19 |
| Figure 22: BER curves vs received power of the TE and TM modes at 1487.18 nm for (a) 10 Gb/s, (b) 20 Gb/s, and channel penalties at (c) 10 Gb/s and (d). | 20 |
| Figure 23: BER curves vs received power of TE and TM modes at 1581.26 nm at (a) 10 Gb/s and (b) 20 Gb/s, and channels power penalties at (c) 10 Gb/s and (d) 20 Gb/s. | 21 |
| Figure 24: BER curves vs received power of the TE and TM modes at (a) 1297.28 nm at 10 Gb/s, (b) Power penalties, (c) at 1403.14 nm at 10 Gb/s and (d) Power penalties. | 21 |

LIST OF TABLES

| | |
|--|----|
| Table 1: Losses summary of the multiband WSS | 8 |
| Table 2: Extinction ratio data for the O, S, C and L-bands. | 10 |
| Table 3: Design parameters of the AWG | 15 |
| Table 4: AWG performance across optical bands. | 19 |

EXECUTIVE SUMMARY

The present scientific deliverable is a part of the Work Package 3 “In-line components design” of the ETN project WON “Wideband Optical Network”, funded under the Horizon 2020 Marie Skłodowska-Curie scheme Grant Agreement 814276.

The document provides details derived from the experimental results regarding a multiband photonic integrated wavelength selective switch and a wideband photonic integrated multiplexer/demultiplexer based on arrayed waveguide gratings. Experimental results highlight the multiband nature of both devices, operating from the O- to the L-band, and the suitability in various wideband optical transmission schemes.

1. WSS and Mux/demux overview

Wavelength selective switches (WSSs) have as a base component a multiplexer and demultiplexer, and optical switching elements that are used, respectively, to split, combine and switch individual optical channels. They are the basic building blocks of more complex components used in optical transmission systems such as reconfigurable optical add drop multiplexers (ROADMs), optical cross connects (OXC) among others. In the following Section 2 of this deliverable a complete experimental characterization of a multiband WSS working in the O, S, C and L-bands is reported. In section 3, we report a wideband polarization insensitive multiplexer/demultiplexer working from the O to the L-bands.

2. Wideband wavelength selective switch

2.1 Introduction

WSS modules are employed in telecom and datacenter networks for spectrum allocation and routing. For fulfilling the requirements of the next generation of optical multiband networks, working from the O to the L-band, an optical multiband switching solution that is low, in cost and power consumption, is required. Possible optical switching solutions should provide these networks with a data-rate, format and protocol transparent technology. The results presented in this deliverable employ a wideband 1 x 2 WSS module in a typical two-degree add-drop, as seen from Figure 1, with a band demultiplexer that separates the multiband *wavelength-division multiplexing* (WDM) signals before the WSSs modules. At the output of the node, a band multiplexer recombines the multiband WDM signals.

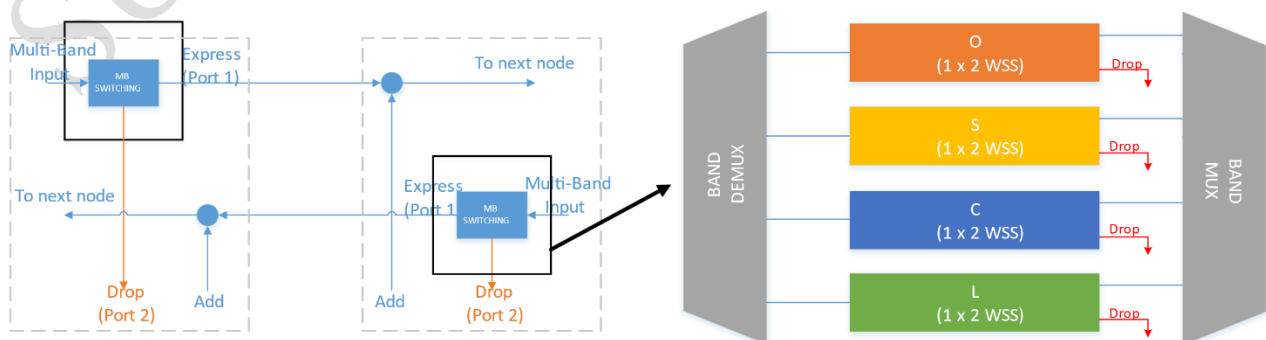


Figure 1: Multi-band 2-degree switching node

The WSS presented in this deliverable worked across the O, S, C and L-bands with some variation in the performance further shown in the following subsections.

2.2 WSS multiband operation

The photonic integrated WSS is a one input two outputs device (1 x 2), based on silica waveguides on a silicon substrate with 1.5% Δ contrast and designed for a channel spacing of 100 GHz in the C-band.

The layout of the fabricated device, as shown in Figure 2, depicts the use of unified *arrayed-waveguide gratings* (AWGs) for the multiplexing and demultiplexing section, contributing for the reduction of device size by reducing the number of AWGs and eliminates potential mismatches between the centre wavelengths of multiple AWGs.

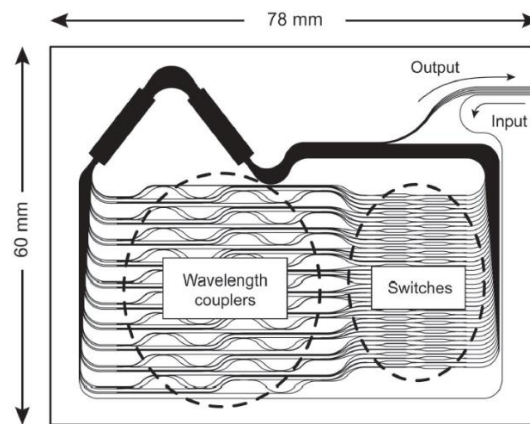


Figure 2: Layout of the fabricated device

Wideband wavelength separation/combining (filtering) is allowed by the cyclic nature of the AWGs [1] and the multiband switching is achieved due to the wideband nature of the thermo-optic effect [2] in Silica. For identifying the channels across the multiband spectrum and assessing the insertion losses for each one, the experimental setup of Figure 3 was employed. In this setup, wideband *amplified spontaneous emission* (ASE) sources were used to create a wideband spectrum for measuring each band. This ASE was in turn used as a back-to-back reference for calculating the insertion losses of the WSS.

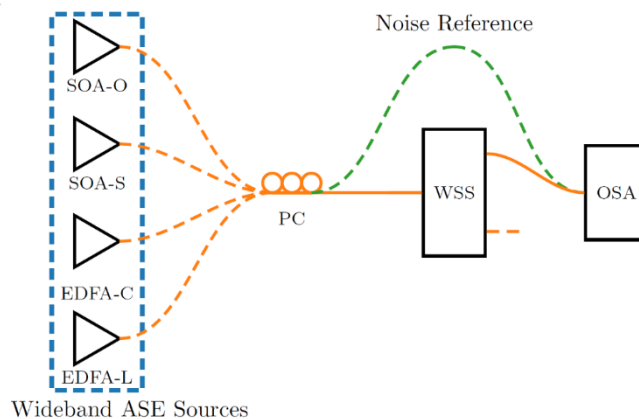


Figure 3: Experimental setup for channel measurement across the multiband spectrum.

In Figure 4, the AWGs operation across the O, S, C and L-bands is shown, where we can also assess the average insertion losses for each channel in each band which in turn is summarized in Table 1.

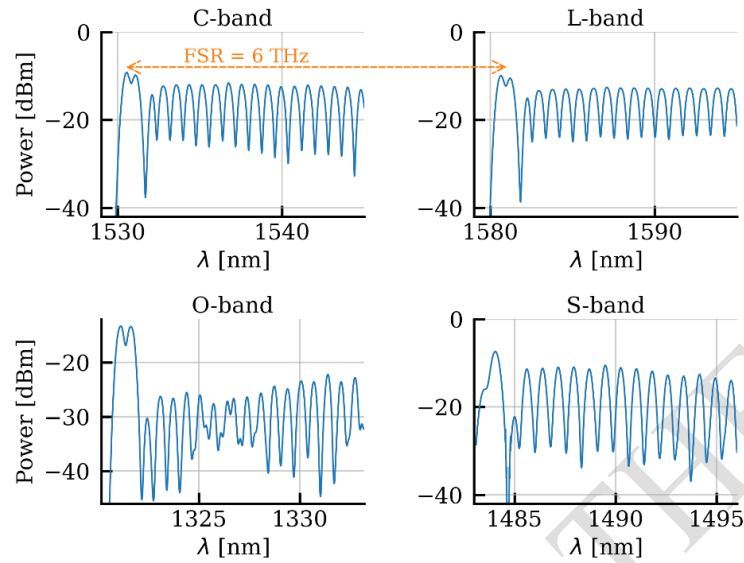


Figure 4: Passband shape of the AWG

| Band | Average Losses | Minimum Loss | Maximum Loss |
|--------|----------------|--------------|--------------|
| O-Band | 23.8 dB | 22.15 dB | 27.6 dB |
| S-Band | 11 dB | 7.76 dB | 16 dB |
| C-Band | 12.7 dB | 9.20 dB | 15.6 dB |
| L-Band | 13 dB | 9.90 dB | 13.8 dB |

Table 1: Losses summary of the multiband WSS

It can be seen from Figure 4 and Table 1 that the O-band experience extra insertion losses when compared to the other bands. These extra losses are due to the wavelength dependence of the wavelength couplers that are part of the WSS. The channels that pass through the wavelength couplers experience extra 13.70 dB losses as highlighted in Figure 5. Wavelength independence of the WSS can be achieved by adopting phase generation couplers, as seen in [3], which demonstrated broadband characteristics from the O- to the L-band, with losses 4 times lower when compared to conventional directional couplers, while also providing low polarization dependent losses.

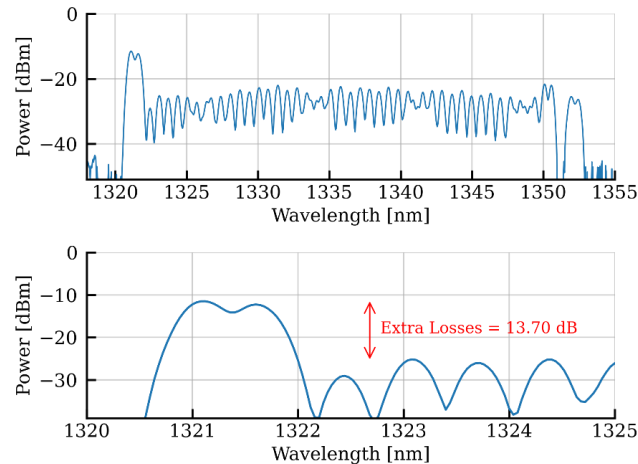


Figure 5: Extra 13.7 dB losses in the O-band due to the wavelength couplers.

From the data presented in Figure 4 the individual channels across the multiband spectrum were analysed, as shown in Figure 6. Average 3 dB bandwidths of 42.74 GHz, 43.48 GHz, 45.3 GHz, and 54.36 GHz, across the O, S, C and L-bands respectively, were numerically found by approximating the passband shape by the sum of two Gaussian functions [4]. This difference in the 3 dB bandwidths across the bands arises from the group index dependency of the *free spectral range* (FSR) as seen in [5].

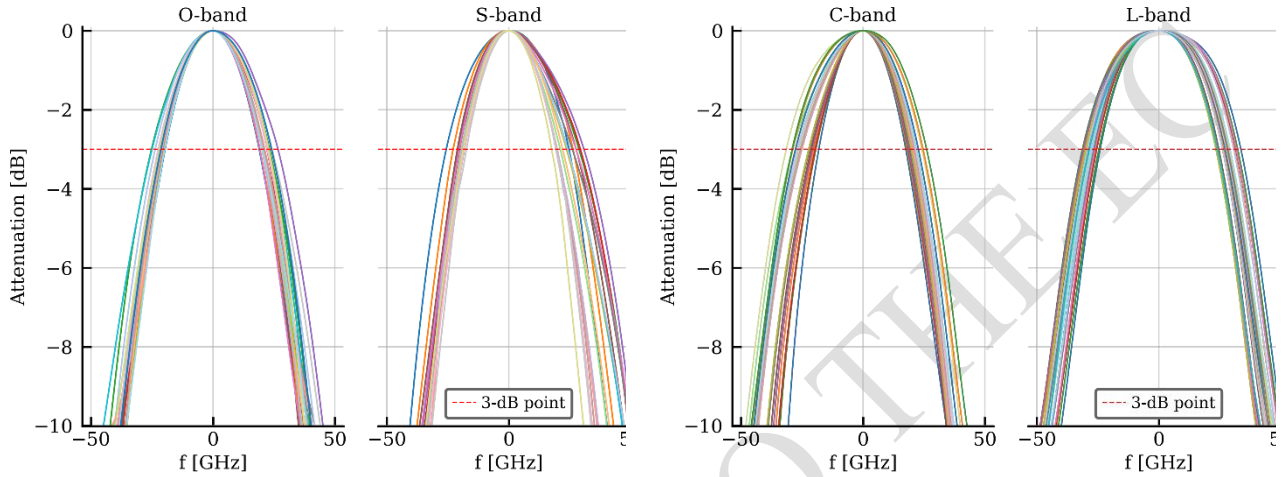


Figure 6- Filter shapes for O, S, C and L-bands.

As stated in Section 2.1, the WSS makes use of thermo-optic phase shifters on Mach-Zehnder interferometers (MZIs) for the switching of individual wavelengths between the two output ports. As seen in [2], [6], this is an adequate choice for wideband operation due to the low variability of the thermo-optic coefficient in Silica glasses across a wide range of wavelengths. This was further confirmed experimentally by testing the power ratio between the two output states, defined here as the *extinction ratio* (ER). The results found are shown in Figure 7 and Table 2.

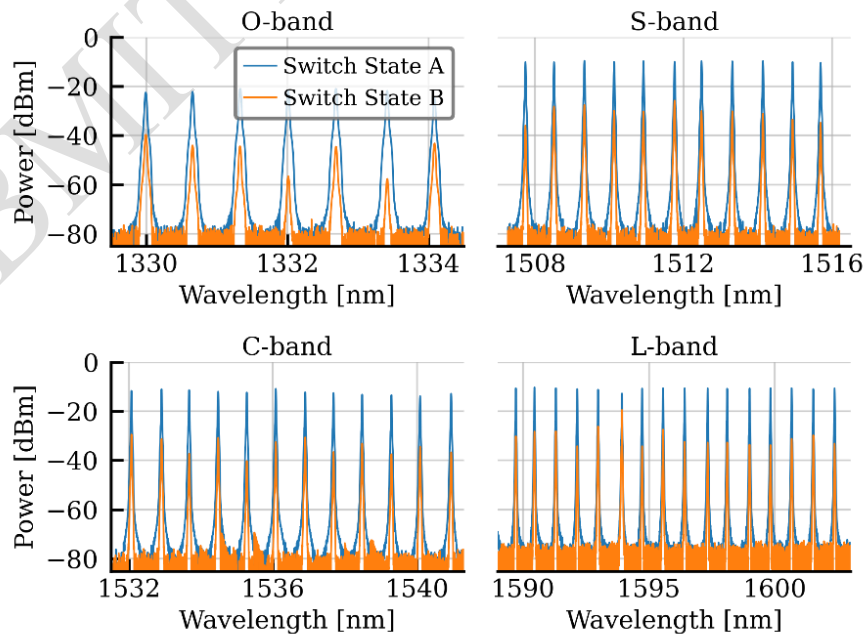


Figure 7: ER across channels in the O, S, C and L-bands.

| Band | Average ER | Minimum ER | Maximum ER |
|--------|------------|------------|------------|
| O-band | 23.62 dB | 11.94 dB | 35.87 dB |
| S-band | 18.21 dB | 6.16 dB | 37.59 dB |
| C-band | 22.59 dB | 14.77 dB | 37.80 dB |
| L-band | 19.38 dB | 4.18 dB | 26.22 dB |

Table 2: Extinction ratio data for the O, S, C and L-bands.

2.3 WSS employed in a wideband data transmission

To verify the possible penalties introduced by a single WSS, two experimental scenarios were considered. First, with *intensity-modulation direct-detection* (IM/DD), and then in a coherent transmission setup.

The experimental setup employed to assess the performance of the WSS in IM/DD is depicted in Figure 8. For the C and L-bands, a broadband *tunable laser-source* (TLS), covering both bands was used as a *continuous-wave* (CW) light source. After the CW source, a polarization controller was used to optimize the state of polarization for the *Mach-Zehnder modulator* (MZM), which was driven at 10 Gb/s and 35 Gb/s NRZ-OOK with a PRBS length of $2^{31} - 1$. After the MZM, an EDFA was used to compensate for the modulator losses and another polarization controller was used to optimize the polarization for the WSS. Following the WSS, a variable optical attenuator was used for the power sweep, an optical spectrum analyser for analysis of the spectral data and the *optical signal-to-noise ratio* (OSNR) of the signal, finally, a photodetector is used to convert the signal from the optical to the electrical domain. For the O-band the same setup applies with some components being exchanged by the O-band counterpart, as for example, the CW source and modulator. In the case of the EDFA it was substituted by a *semiconductor optical amplifier* (SOA) and the PD was exchanged by a high *sensitivity avalanche photodetector* (APD).

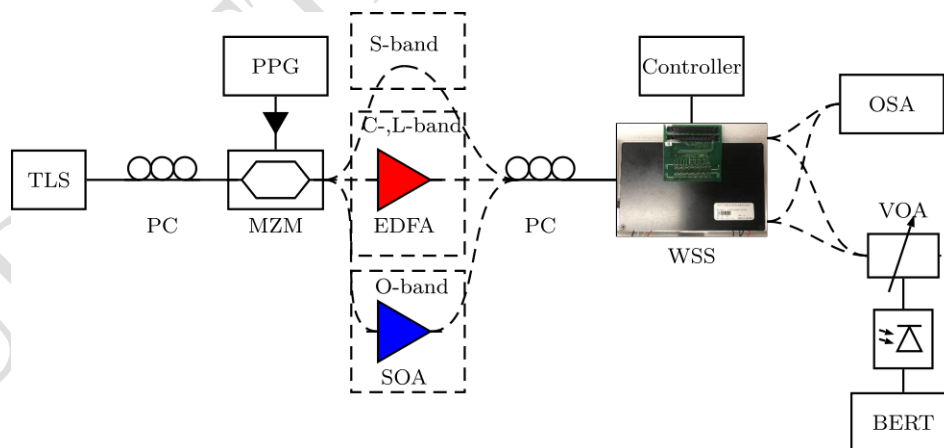


Figure 8: NRZ-OOK Experimental setup.

In Figure 9, the bit error rate (BER) results for the O and S-band at 10 Gb/s are shown. In the case of the O-band, at $\text{BER} = 10^{-9}$ the maximum penalty of 3.2 dB occurred at the channel centred at $\lambda = 1300.06$ nm whereas in the S-band case the maximum power penalty was at most 0.8 dB.

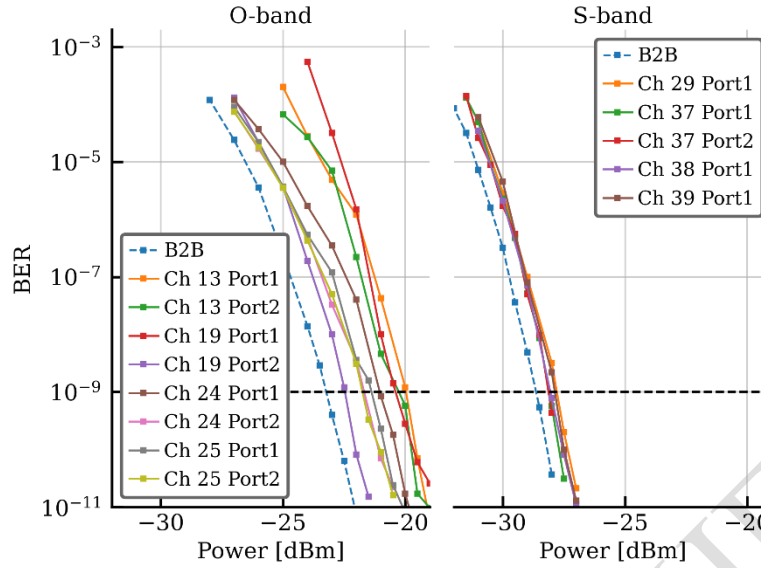


Figure 9: Bit error rate results with 10 Gb/s NRZ-OOK data for the O and S-band.

In Figure 10, the BER curves for the C and L-band at 35 Gb/s are shown. In the case of the C-band the penalty was 2 dB at $\text{BER} = 10^{-9}$ for most of the tested channels, and in the case of the L-band the penalty ranged from 0.7 dB to 3.5 dB, mainly due to slightly variations between the AWG channel shapes and deviations from the 100 GHz channel spacing.

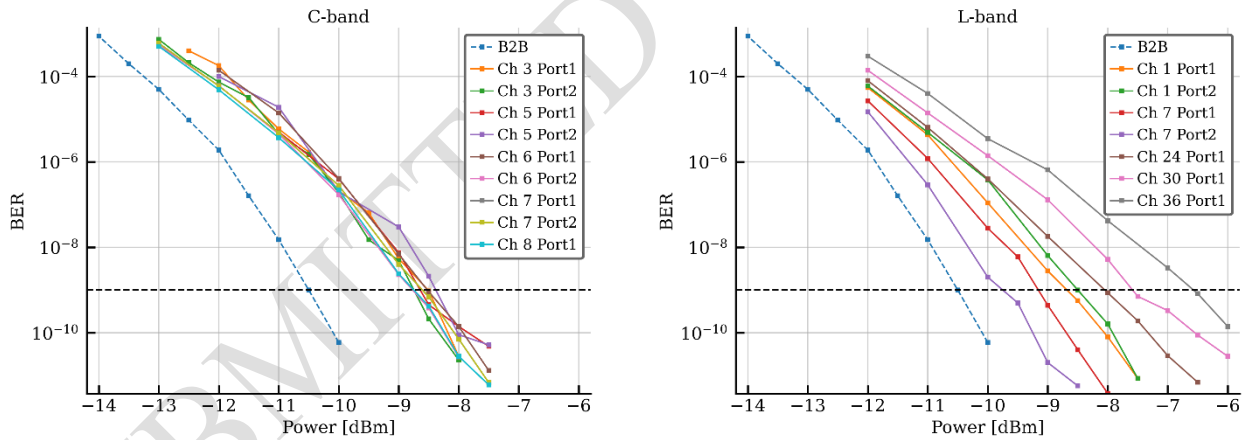


Figure 10: BER results with 35 Gb/s in the C and L-band.

In the coherent transmission experimental validation, as depicted in the experimental setup of Figure 11, a TLS was set to wavelengths 1515.74 nm and 1516.54 nm in the S-band, from 1532.75 nm to 1553.75 nm with 0.8 nm spacing in the C-band and from 1583.71 nm to 1599.60 nm with also 0.8 nm in the L-band. After the TLS, an EDFA was used to amplify the CW light that will be also used as local oscillator to the coherent receiver. Offline, PCG64 pseudo-random data streams containing 2^{16} quadrature amplitude modulation (QAM) symbols are pulse-shaped using a root-raised-cosine filter with roll-off $\beta = 0.01$ and uploaded to a 100 GSa/s digital-to-analog converter (DAC). The DAC outputs are connected to RF amplifiers which in turn are connected to the IQ optical modulator. After the modulator, the signal is fed into the WSS, which is remotely controlled according to the channel being tested.

A noise loading stage consisting of S-band SOAs, C and L-band EDFAs connected to a variable optical attenuator, was used for the OSNR sweep. The coherent receiver consisted of the already mentioned local oscillator, a 90-degree hybrid and 2 balanced photodiodes. The detected signal is digitized by an 80 GSa/s analog-to-digital converter (ADC) and further processed by the offline receiver DSP, consisting of matched filtering, MIMO equalization with in-loop blind phase search and performance metrics evaluation.

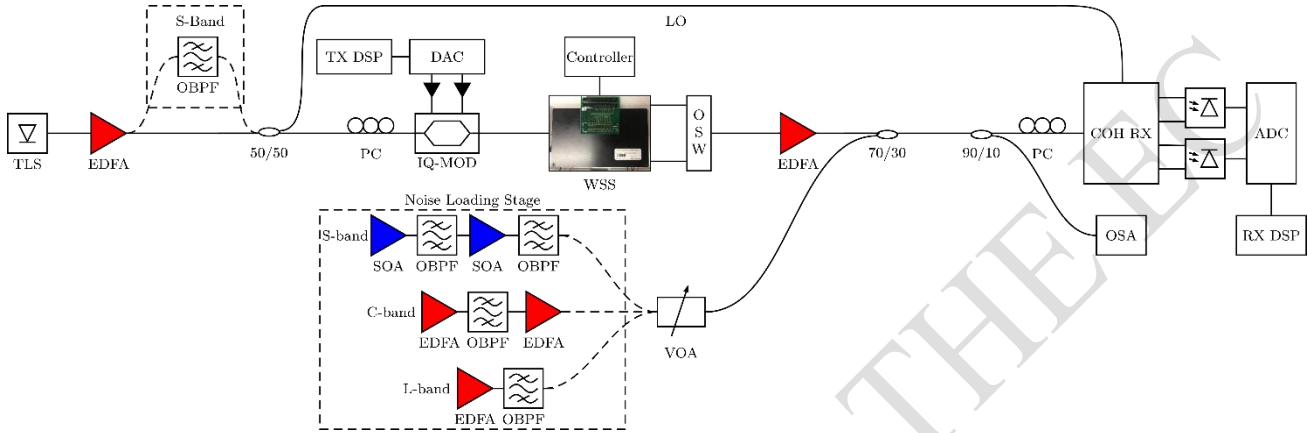


Figure 11: Schematic of the coherent experimental setup.

The WSS performance was evaluated with 64-QAM 33.3 Gb/s data while sweeping the OSNR from the minimum achievable level, limited by the maximum output power of the respective noise loading stage, to the maximum OSNR value, where most of the noise power was attenuated by a VOA.

In Figure 12, as a figure of merit of the performance the *normalized generalized mutual information* (NGMI) is used, as it has been shown to provide consistent post FEC BER predictions across different conditions and modulation formats [7]. Considering the FEC overhead for LDPC codes concatenated with a staircase code [8], the NGMI of 0.88 and 0.92 shown in Figure 11 corresponds to a net data-rate of 161.84 Gb/s and 169.83 Gb/s, respectively.

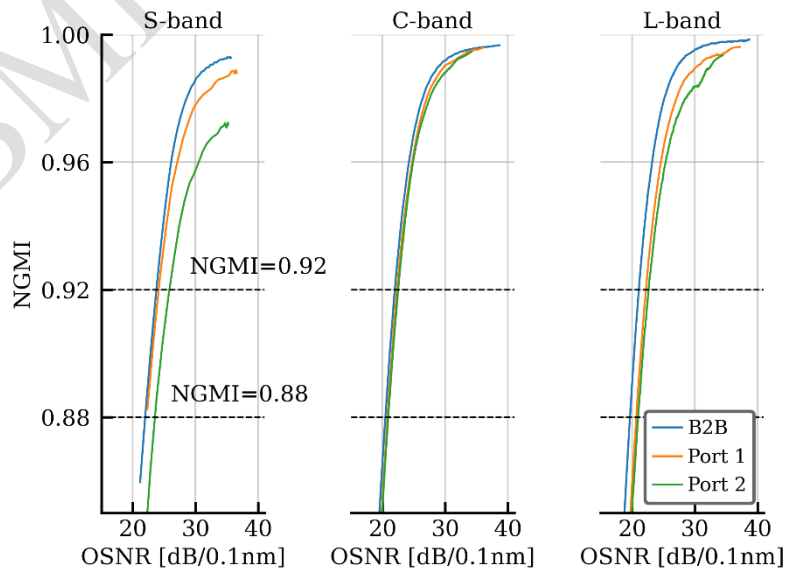


Figure 12: Averaged NGMI and BER for the S, C and L-bands.

Further comparing the NGMI performance across each band, we can see in Figure 13 the OSNR penalty for each NGMI value when comparing to the back-to-back counterparts. It was verified that for the C-band case, the penalty was always smaller than 1 dB for both output ports, for the L-band greater than 1 dB for most of the tested channels and in the S-band ranging from 0.6 dB to 2.2 dB.

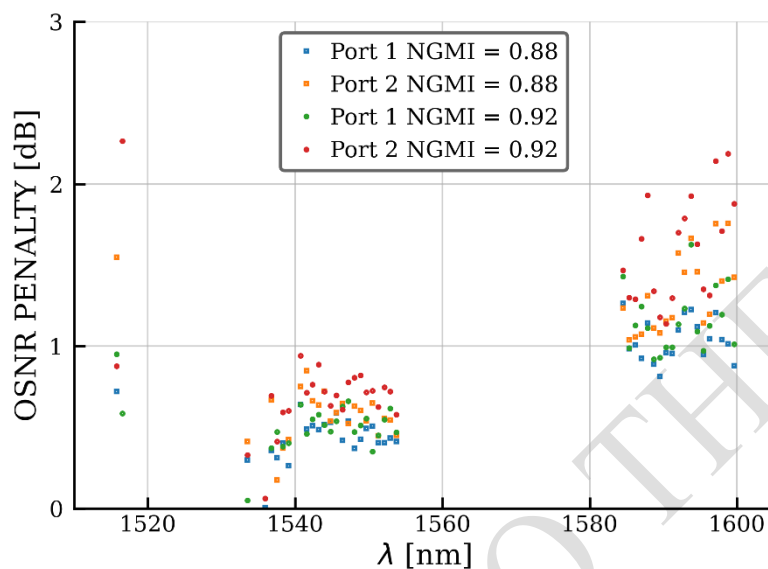


Figure 13: OSNR penalty from the S to the L-band for NGMI values of 0.88 and 0.92, and corresponding net data-rates of 161.84 Gb/s and 169.83 Gb/s respectively.

3. Ultrawide-band mux/demux based on polarization insensitive arrayed waveguide gratings

3.1 Introduction

To multiplex (mux) and demultiplex (demux) different wavelengths in multiband systems, ultra-wide band AWGs is one of the key components. Moreover, AWGs are key components for realizing more complex photonic integrated components such as WSSs [9] that are used for dynamic network operation. An example of the AWG employed in a WSS is shown in the previous section and in Figure 14.

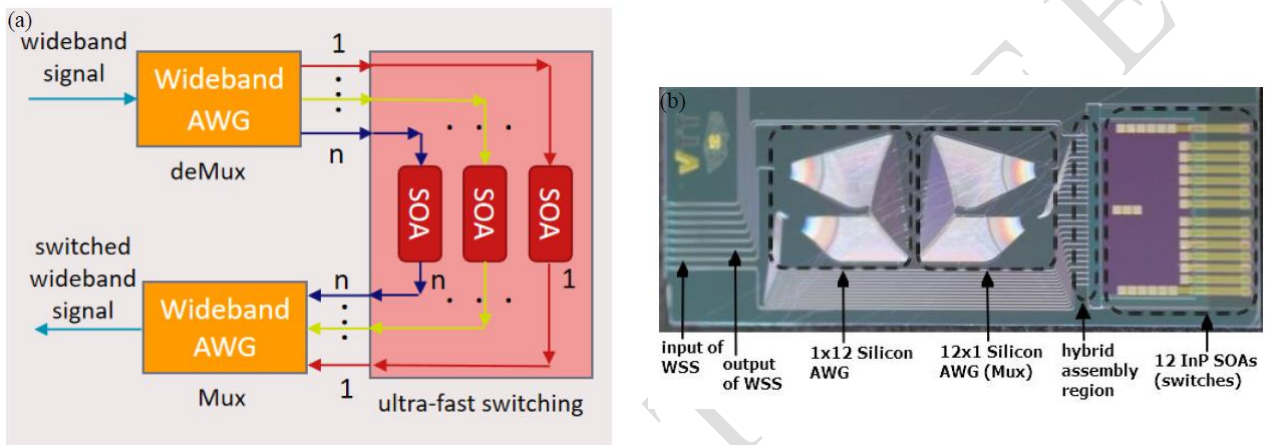


Figure 14: (a) Schematic of hybrid WSS. (b) Micrograph of the fabricated hybrid-assembly 1 x 1 WSS

Many AWGs have been fabricated and reported on different integrated photonics platforms, such as Silica, InP and SOI. One of the important AWG features is the polarization independent operation. Different methods have been investigated to minimize the *polarization dependent losses* (PDL) and *polarization dependent wavelength shift* (PDWS) of AWGs such as, inserting a half-wave plate [10] at the centre of the AWG, splitting or converting polarizations [11], [12], among other methods. In this deliverable, the design, fabrication, and characterization of the ultra-wideband 1 x 12 AWG with 100 GHz channel spacing on a 3- μm SOI platform will be shown.

3.2 Design and Fabrication

3- μm thick Silicon waveguides are an attractive approach for ultra-low loss, ultra-wideband and polarization independence because the thick waveguide core can confine the optical mode field completely, which results in ultra-low propagation loss, in the range of 0.1 dB/cm. Furthermore, by controlling the relative waveguide dimensions under the single mode condition [13], the Silicon waveguide can be designed to offer single-mode operation and down-to-zero birefringence over a wide wavelength range, from 1.2 μm to 4 μm . The detailed structure of the 3- μm Silicon strip waveguide is shown in Figure 15.

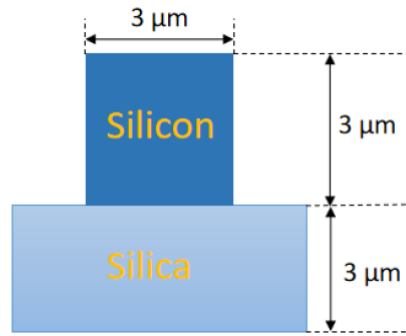


Figure 15: Detailed structure of the 3- μm Silicon strip waveguide.

The designed AWG is composed of input/output waveguides, input/output star couplers and an array of single-mode 3- μm waveguides. The operating principle – as a demultiplexer – is briefly described as follows: (i) the optical signal with different wavelengths coming from the input waveguide enters the input star coupler and the diverging light beam is distributed over the arrayed waveguides; (ii) after propagating through the waveguides array, the different wavelengths have a different optical path length and interfere constructively in the output star coupler; (iii) finally, the different wavelengths focuses on different positions upon the circle of the output coupler and the output positions depends on the optical path difference. Therefore, the effective refractive index difference between the TE and TM modes in the arrayed waveguides lead to polarization dependent wavelength shift and polarization dependent losses for the fixed-position output channel. By employing the polarization independent waveguides, whose optical field distribution is almost identical for the TE and TM polarizations, the PDWS and PDL are minimized.

The parameters of the designed AWG are shown in Table 3. It can be seen from this table that to decrease the insertion losses and crosstalk levels, 100 arrayed waveguides are employed with 5- μm width and 150- μm length tapers connecting to the star couplers, and the physical spacing between output channels is set to 1 μm .

| | |
|-------------------------------------|----------|
| Diffraction order | 96 |
| Number of arrayed waveguides | 100 |
| Channel spacing | 100 GHz |
| Channel number | 12 |
| FSR | 2 THz |
| PDWS | 0.001 nm |
| PDL | 0.1 dB |
| Insertion Losses | -0.70 dB |
| Crosstalk | < 50 dB |

Table 3: Design parameters of the AWG

As stated before, one of the key characteristics of the AWG that allow multiband operation is the FSR. The designed AWG has a central wavelength of 1547.61 nm with a FSR of 2 THz. The FSR and ultrawide band low-loss waveguides allow the AWG to multiplex and demultiplex optical signals from the O to the L-band. Even though the number of arrayed waveguides is large, the size of the AWG is quite compact (< 6.6 mm²) due to the low radius of the Euler bends. The layout and the designed response of the AWG is shown in Figure 16.

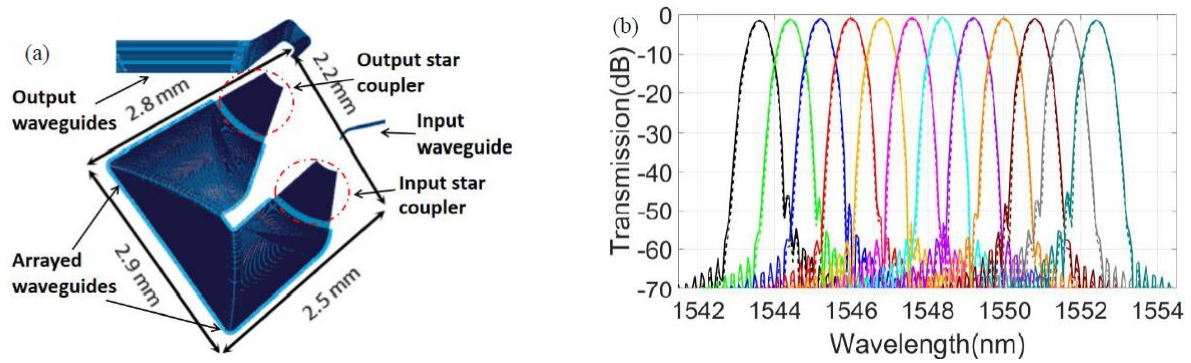


Figure 16: (a) AWG Layout. (b) Simulated 12 channels output for TE and TM modes in the C-band.

The AWGs were fabricated on a SOI wafer with a 3- μm thick top silicon layer and a 3- μm thick buried oxide layer. The pattern was transferred to the wafer by i-line technology, and a double-step etching process was implemented to form the rib-strip waveguide structure by inductively coupled plasma technology. The end facets of the input and output waveguides were covered with SiN layer, acting as an anti-reflection coating to reduce the coupling losses between waveguides and fibres. Finally, a 500-nm cladding SiO_2 layer was grown by *plasma enhanced chemical vapor deposition* (PECVD) technology to protect the AWG. The fabricated AWG is shown on the micrograph in Figure 17.

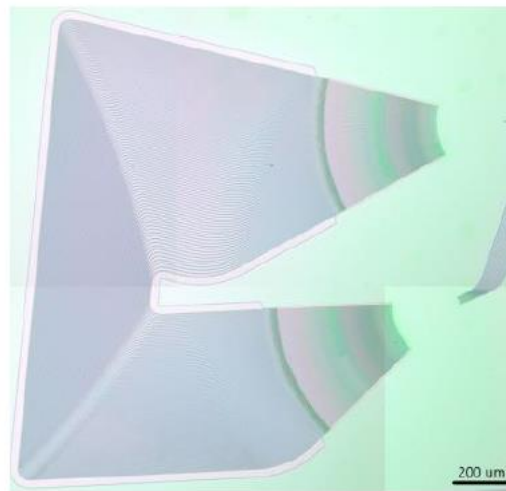


Figure 17: Micrograph of the fabricated AWG.

3.3 Experimental characterization

The experimental setup used to characterize the fabricated AWG is shown in Figure 18. First, a tunable laser source was used to sweep the spectrum from the O to the L-band, the polarization controller is employed to adjust the state of polarization at the input of the AWG to measure the PDL and PDWS. The AWG is mounted on a chip holder, connected to a vacuum pump for stabilization and no methods for temperature control were used. Two 6-axis stages are used to adjust the lensed fibres for optimal alignment between the fibres the input/output waveguides of the AWG.

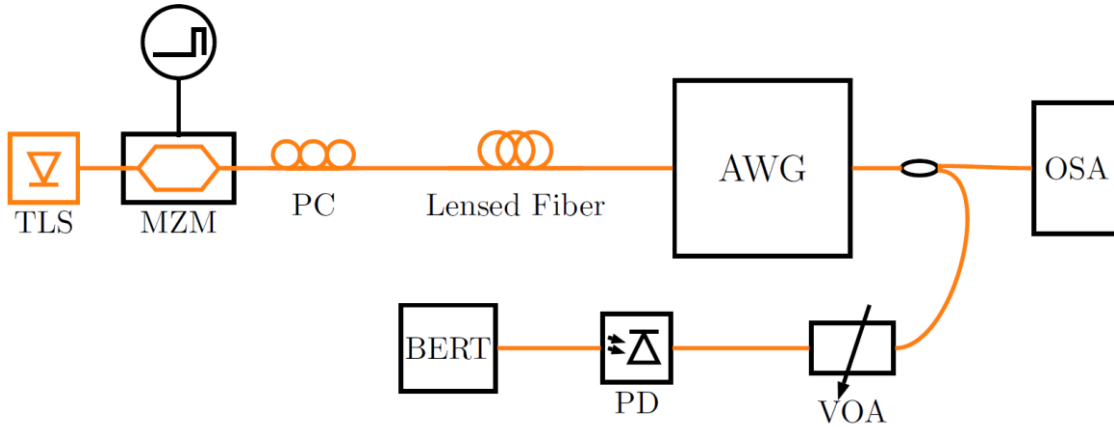
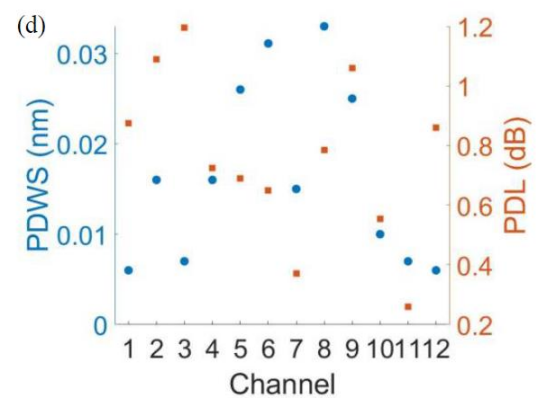
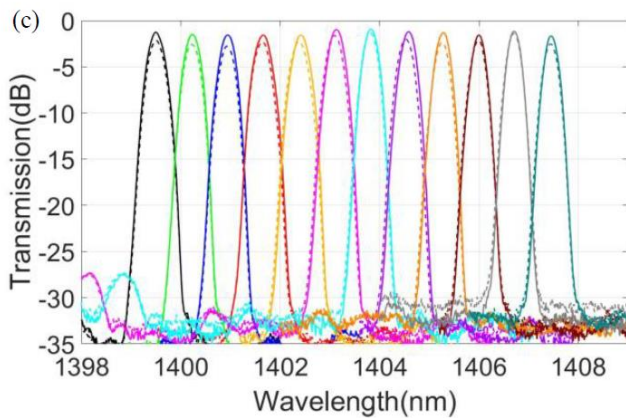
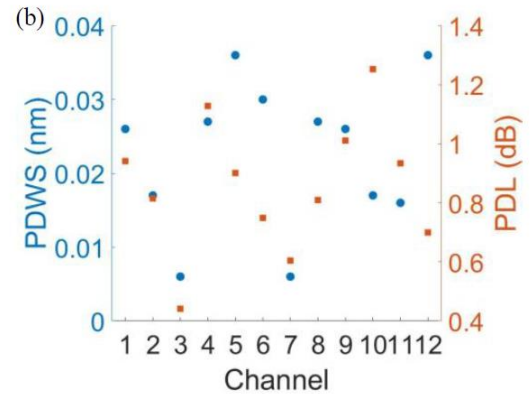
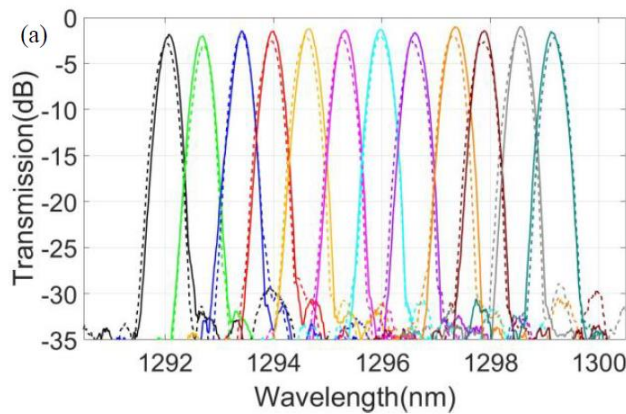


Figure 18: Experimental setup for characterization of the 1 x 2 PI AWG.

First, the PDLs, PDWs and channel shapes of all 12 channels in the O, E, S, C and L-band were measured as shown in Figure 19 and Figure 20, with the solid curve being the TE mode and the dashed the TM mode. Not considering the coupling losses of 2 dB per facet, the lowest insertion loss of approximately -0.82 dB was measured for the TE mode and -1.12 dB for the TM mode in the C-band. The measured average crosstalk of the 12 channels of the AWG across all bands ranged from -33 dB to -35 dB and the maximum wavelength shift is 41 pm in the S-band. The PDLs ranged from 0.18 dB to 1.27 dB across all bands. The results are summarized in Table 4.



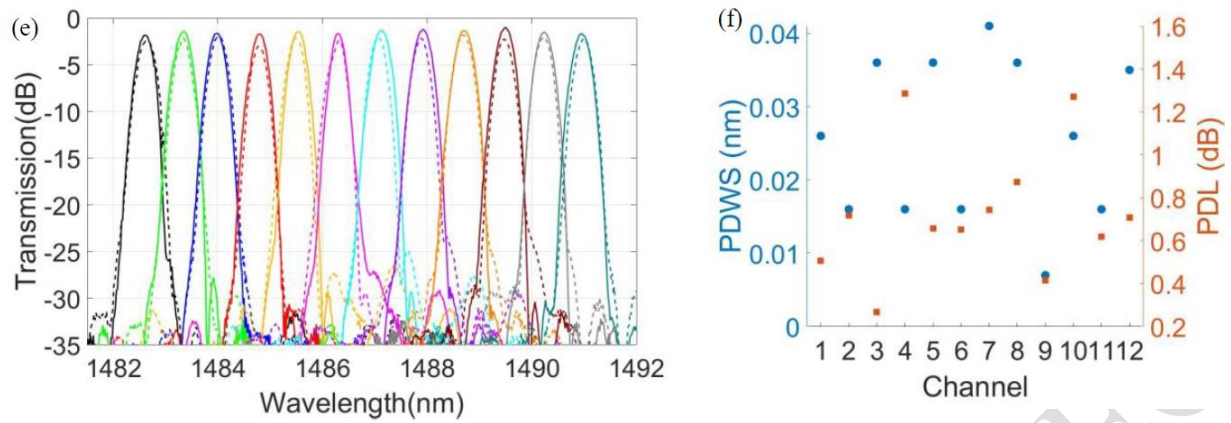


Figure 19: Measured output spectra of 12 channels at the O, E, S band, and the respective PDWs and PDLs.

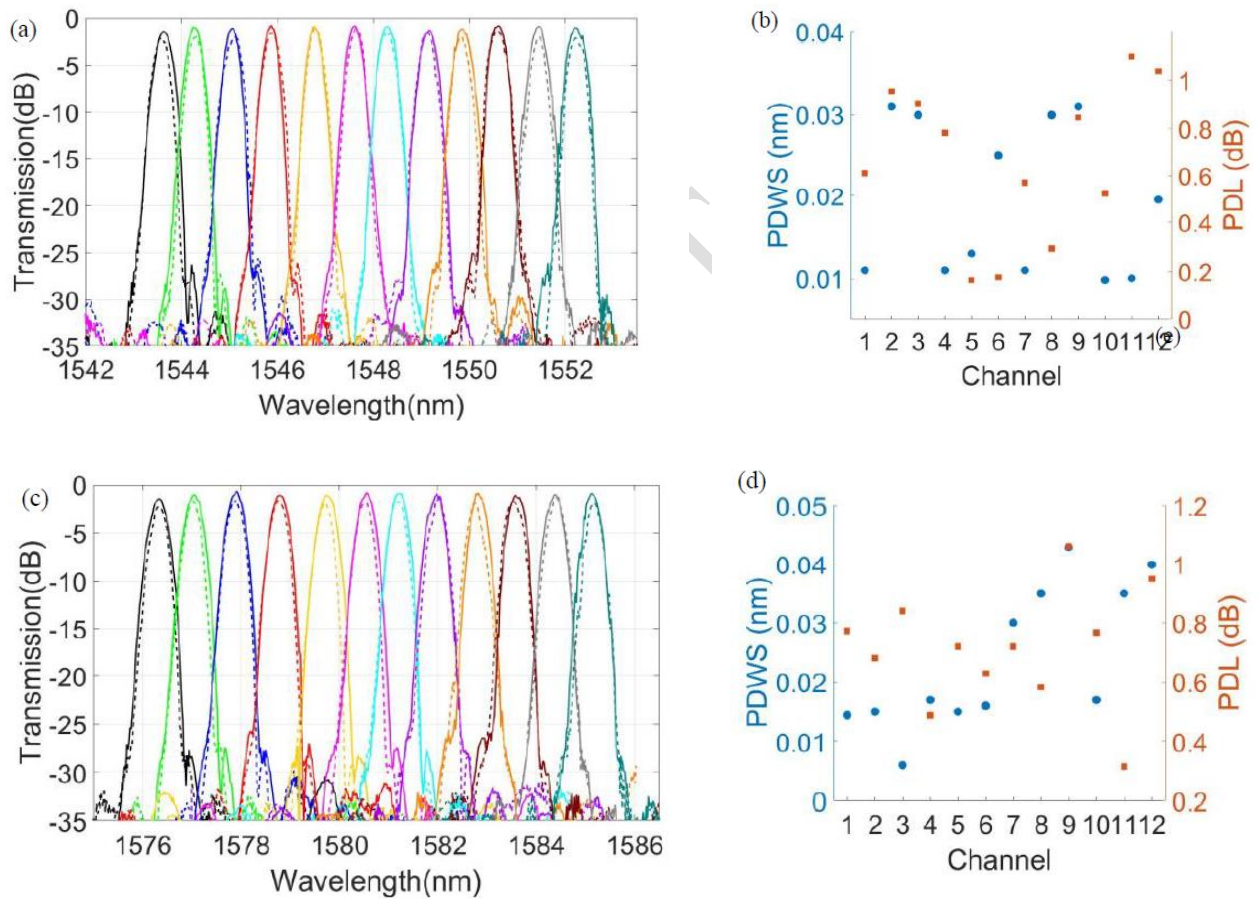


Figure 20: Measured output spectra of 12 channels at the C and L-band and the respective PDWs and PDLs.

| Band | IL (dB) TE/TM | Avg. Crosstalk | PDL (dB) | PDWS | Channel non- uniformity | 3-dB BW | Channel Spacing |
|--------|------------------|-------------------|-------------|---------|-------------------------------|---------|--------------------|
| O-band | -0.91/-1.52 | -34 dB | 0.25 ~ 1.05 | 6~36 pm | 1.50 dB | 0.32 nm | 0.65 nm |
| E-band | -0.94/-1.36 | -33 dB | 0.26 ~ 1.23 | 7~38 pm | 0.92 dB | 0.34 nm | 0.72 nm |
| S-band | -0.93/-1.31 | -33 dB | 0.24 ~ 1.27 | 8~41 pm | 0.65 dB | 0.34 nm | 0.75 nm |
| C-band | -0.82/-1.12 | -35 dB | 0.18 ~ 1.09 | 8~33 pm | 0.75 dB | 0.35 nm | 0.79 nm |
| L-band | -0.85/-1.40 | -33 dB | 0.31~1.06 | 7~40 pm | 0.80 dB | 0.35 nm | 0.81 nm |

Table 4: AWG performance across optical bands.

The experimental results shown in Figures 19 and 20 and Table 4 confirm the similar AWG performance across all bands as a wideband mux/demux, with low insertion losses, low crosstalk, and a low polarization sensitivity.

For the data transmission results with NRZ-OOK at 10 Gb/s, 20 Gb/s and 35 Gb/s with PRBS length of $2^{31} - 1$, the obtained measured results are shown in Figure 21 to 24.

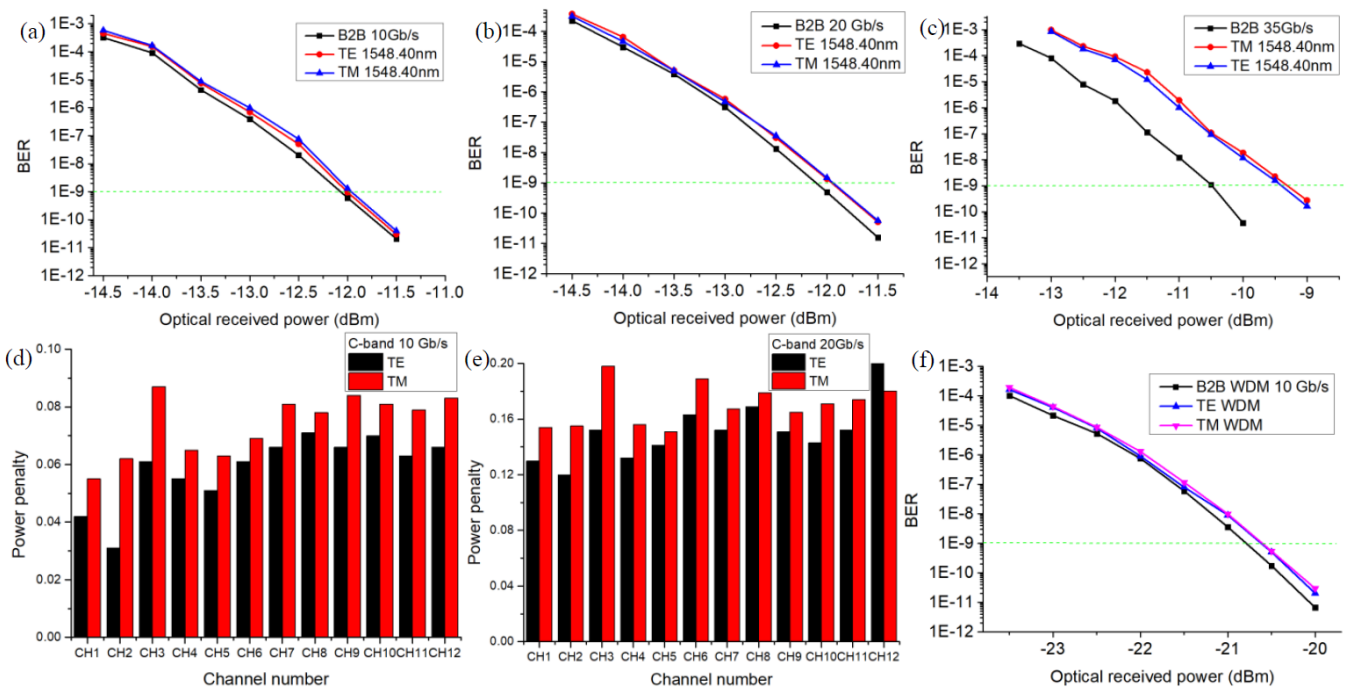


Figure 21: BER curves vs received power of the TE and TM modes at 1548.40 nm for (a) 10 Gb/s, (b) 20 Gb/s and (c) 35 Gb/s, and channel penalties at (d) 10 Gb/s, (e) 20 Gb/s and (f) BER curve of TE and TM modes for WDM 10 Gb/s signal.

In Figure 21, it was measured at the C-band error-free operation in all channels with a power penalty at $BER = 10^{-9}$ smaller than 0.17 dB for 10 Gb/s and 20 Gb/s data rates. For 35 Gb/s, the power penalty at 10^{-9} increases to 0.8 dB due to the limited 3dB bandwidth of the AWG. It can also be seen

in Figure 21 (d) and (e) that the power penalties are smaller than 0.2 dB for both polarizations for all tested channels.

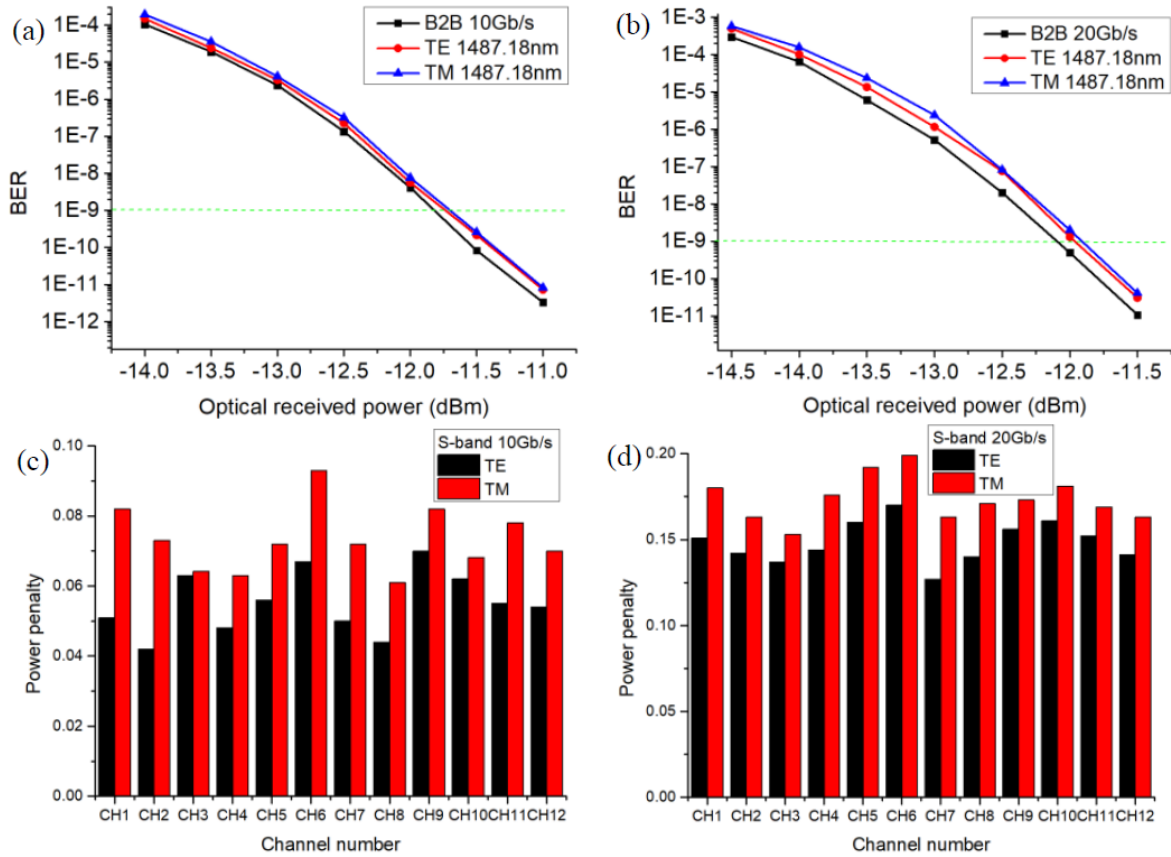


Figure 22: BER curves vs received power of the TE and TM modes at 1487.18 nm for (a) 10 Gb/s, (b) 20 Gb/s, and channel penalties at (c) 10 Gb/s and (d).

For the S-band, Figure 22, similar penalties were measured. For 10 Gb/s at $\lambda = 1487.18$ nm the penalties were smaller than 0.1 dB for both polarizations and in the case of 20 Gb/s at the same wavelength the penalties were smaller than 0.2 dB. The same was measured in the L-band at $\lambda = 1581.26$ nm, Figure 23, error free operation for all channels with penalties smaller than 0.1 dB and 0.2 dB for 10 Gb/s and 20 Gb/s respectively and for both polarizations.

In the case of the O-band and E-band, shown in Figure 24, due to the lack of higher data rate modulators at this part of the spectrum the channels were tested only at 10 Gb/s for both polarizations. In the O-band, $\lambda = 1297.98$ nm, the penalties were always smaller than 0.1 dB, as seen from Figure 24 (b). The same was verified for the E-band, channel at $\lambda = 1403.14$ nm, with the penalties always smaller than 0.1 dB for both polarizations states.

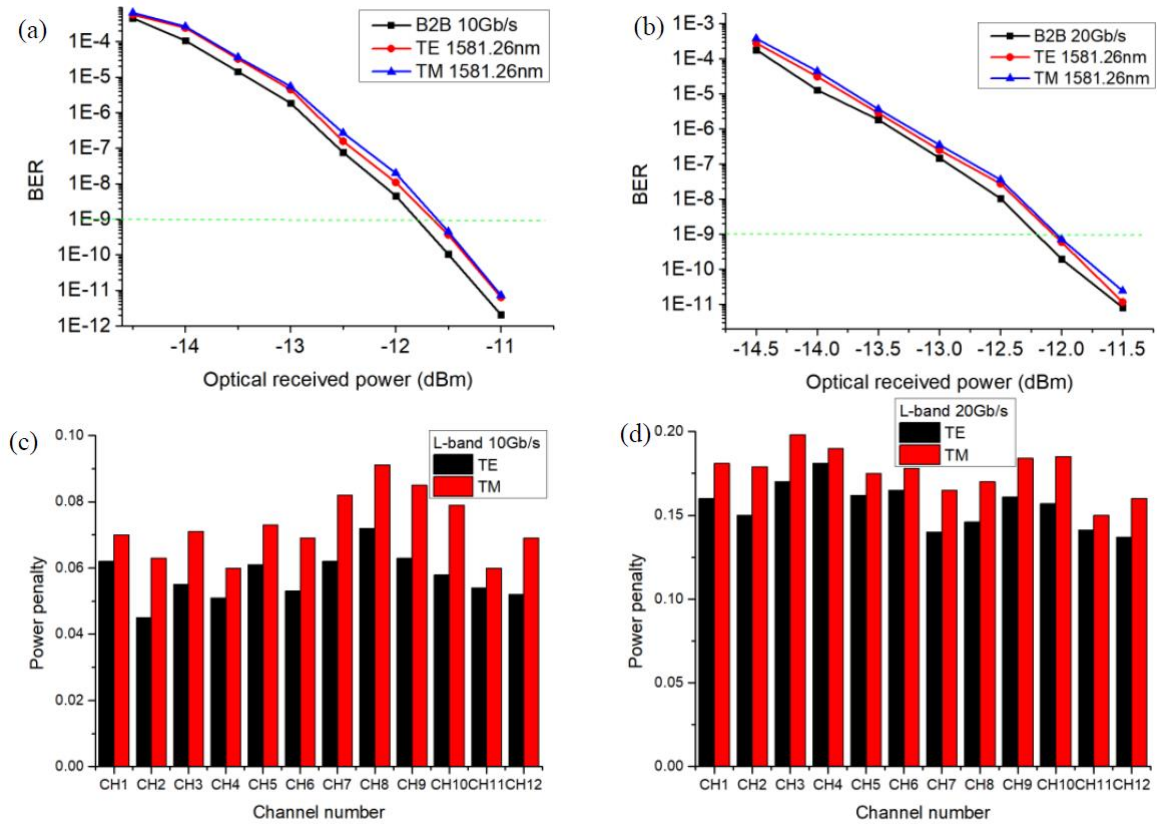


Figure 23: BER curves vs received power of TE and TM modes at 1581.26 nm at (a) 10 Gb/s and (b) 20 Gb/s, and channels power penalties at (c) 10 Gb/s and (d) 20 Gb/s.

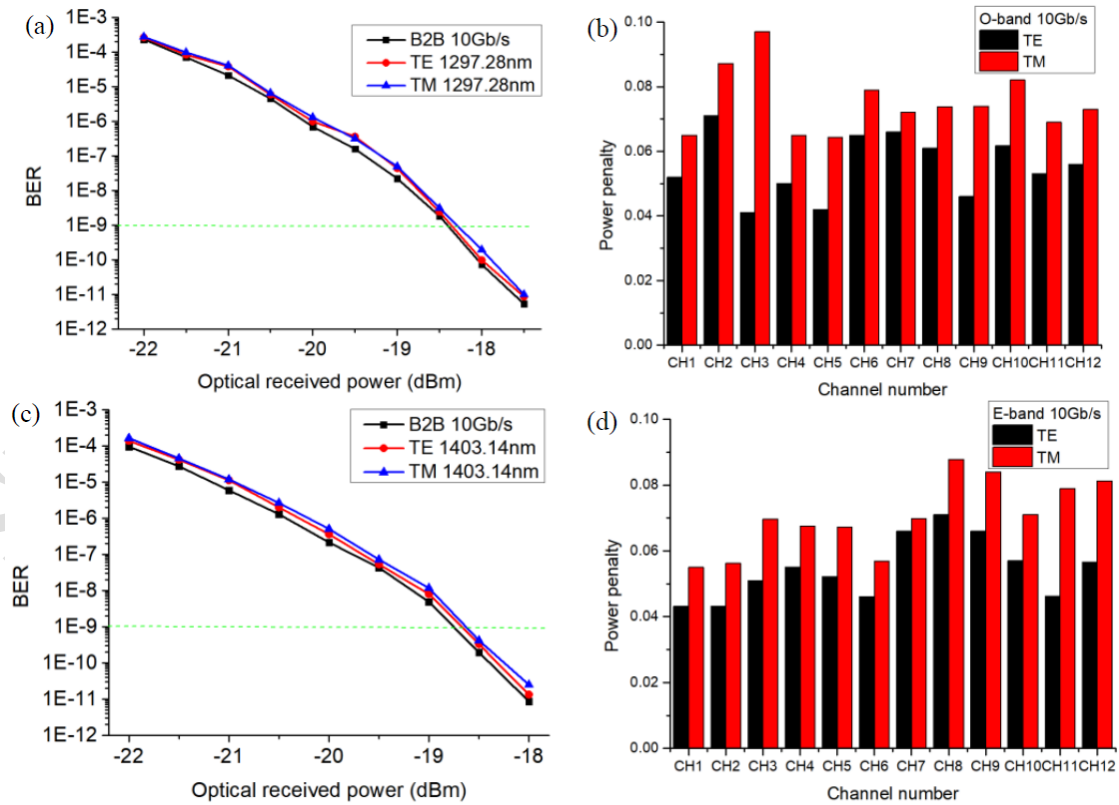


Figure 24: BER curves vs received power of the TE and TM modes at (a) 1297.28 nm at 10 Gb/s, (b) Power penalties, (c) at 1403.14 nm at 10 Gb/s and (d) Power penalties.

4. Conclusions

In this deliverable we presented the complete multiband (O to the L-band) experimental validation of a photonic integrated WSS and ultrawide-band polarization insensitive mux/demux AWG.

For both devices, extensive technical characterization was conducted to assess the multiband performance of the devices, showing adequate wideband operation for both devices. Furthermore, experimental data transmission showed the WSS operating from 10 to 35 Gb/s IM/DD scheme and with a coherent transmission scenario with net data-rates of 169.83 Gb/s with small power and OSNR penalties in all bands and channels. For the mux/demux AWG it was also shown the low insertion losses of the device and small polarization dependent losses (<0.2 dB) and experimental multiband data transmission showed power penalties smaller than 0.1 dB, 0.2 dB and 0.8 dB for 10 Gb/s, 20 Gb/s and 35 Gb/s, respectively.

5. REFERENCES

- [1] M. K. Smit, A. Member, and C. van Dam, "PHASAR-Based WDM-Devices :," vol. 2, no. 2, pp. 236–250, 1996.
- [2] G. Ghosh, "Temperature Dispersion of Refractive Indexes in Some Silicate Fiber Glasses," *IEEE Photonics Technology Letters*, vol. 6, no. 3, pp. 431–433, 1994, doi: 10.1109/68.275509.
- [3] T. Watanabe, T. Mizuno, Y. Hashizume, and T. Takahashi, "Silica-based PLC 1×N switch for all wavelength bands," *Optics InfoBase Conference Papers*, no. 2, pp. 14–16, 2014, doi: 10.1364/ofc.2014.th1i.5.
- [4] R. Kraemer *et al.*, "Multi-band photonic integrated wavelength selective switch," *Journal of Lightwave Technology*, vol. 39, no. 19, pp. 6023–6032, Oct. 2021, doi: 10.1109/JLT.2021.3096045.
- [5] Z. Liu and J. Li, "Modeling and design of arrayed waveguide gratings," *CAR 2010 - 2010 2nd International Asia Conference on Informatics in Control, Automation and Robotics*, vol. 3, no. 4, pp. 339–341, 2010, doi: 10.1109/CAR.2010.5456702.
- [6] "Thermo-Optic Coefficients," *Handbook of Optical Constants of Solids*, pp. 115–261, 1997, doi: 10.1016/b978-012544415-6.50150-3.
- [7] A. Alvarado, E. Agrell, D. Lavery, R. Maher, and P. Bayvel, "Replacing the Soft-Decision FEC Limit Paradigm in the Design of Optical Communication Systems," *Journal of Lightwave Technology*, vol. 33, no. 20, pp. 4338–4352, 2015, doi: 10.1109/JLT.2015.2450537.
- [8] A. Alvarado, T. Fehenberger, B. Chen, and F. M. J. Willems, "Achievable Information Rates for Fiber Optics: Applications and Computations," *Journal of Lightwave Technology*, vol. 36, no. 2, pp. 424–439, 2018, doi: 10.1109/JLT.2017.2786351.
- [9] N. Tessema *et al.*, "Modularly and Hybrid Integrated SiPh/InP Wavelength Blocker Switch for Metro Networks," *2020 European Conference on Optical Communications, ECOC 2020*, pp. 3–6, 2020, doi: 10.1109/ECOC48923.2020.9333290.
- [10] Z. Zhang, N. Mettbach, and C. Zawadzki, "Polymer-based photonic toolbox: passive components, hybrid integration and polarisation control," *IET Optoelectronics*, vol. 5, no. 5, pp. 226–232, Oct. 2011.
- [11] Q. Han, J. St-Yves, Y. Chen, M. Ménard, and W. Shi, "Polarization-insensitive silicon nitride arrayed waveguide grating," *Optics Letters*, vol. 44, no. 16, p. 3976, Aug. 2019, doi: 10.1364/ol.44.003976.
- [12] Y. Onawa, H. Okayama, D. Shimura, H. Takahashi, H. Yaegashi, and H. Sasaki, "Polarisation insensitive wavelength de-multiplexer using arrayed waveguide grating and polarisation rotator/splitter," *Electronics Letters*, vol. 55, no. 8, pp. 475–476, 2019, doi: 10.1049/el.2018.8106.
- [13] T. Aalto *et al.*, "Open-Access 3-μm SOI Waveguide Platform for Dense Photonic Integrated Circuits," *IEEE Journal of Selected Topics in Quantum Electronics*, vol. 25, no. 5, Sep. 2019, doi: 10.1109/JSTQE.2019.2908551.